Report No: TRC-EM-CAB-9301

HIGH-FREQUENCY TECHNIQUES FOR RCS PREDICTION OF PLATE GEOMETRIES AND A PHYSICAL OPTICS/EQUIVALENT CURRENTS MODEL FOR THE RCS OF TRIHEDRAL CORNER REFLECTORS

Semiannual Progress Report

PART A

Constantine A. Balanis and Lesley A. Polka

August 1, 1992 - January 31, 1993

PART B

Constantine A. Balanis and Anastasis C. Polycarpou

August 1, 1992 - January 31, 1993

**Telecommunications Research Center
College of Engineering and Applied Science
Arizona State University
Tempe,   AZ 85287-7206**

HIGH-FREQUENCY TECHNIQUES FOR RCS PREDICTION OF PLATE GEOMETRIES AND A PHYSICAL OPTICS/EQUIVALENT CURRENTS MODEL FOR THE RCS OF TRIHEDRAL CORNER REFLECTORS

Semiannual Progress Report

PART A

Constantine A. Balanis and Lesley A. Polka

August 1, 1992 - January 31, 1993

PART B

Constantine A. Balanis and Anastasis C. Polycarpou

August 1, 1992 - January 31, 1993

Telecommunications Research Center
College of Engineering and Applied Science
Arizona State University
Tempe, AZ 85287-7206

Abstract

Part I of this report continues the investigation, initiated in previous reports, of scattering from rectangular plates coated with lossy dielectrics. The hard polarization coefficients given in the last report are incorporated into a model, which includes second- and third-order diffractions, for the coated plate. Computed results from this model are examined and compared to measured data. A breakdown of the contribution of each of the higher-order terms to the total RCS is given. The effectiveness of the UTD model in accounting for the coating effect is investigated by examining a Physical Optics (PO) model which incorporates the equivalent surface impedance approximation used in the UTD model. The PO, UTD, and experimental results are compared.

Part II of this report presents a radar cross section (RCS) model, based on Physical Optics (PO) and the Method of Equivalent Currents (MEC), for a trihedral corner reflector. PO is used to account for the reflected fields, while MEC is used for the diffracted fields. Single, double, and triple reflections and first-order diffractions are included in the model. A detailed derivation of the E_θ-polarization, monostatic RCS is included. Computed results are compared with finite-difference time-domain (FDTD) results for validation. The PO/MEC model of this report compares very well with the FDTD model, and it is a much faster model in terms of computational speed.

1

I. HIGH-FREQUENCY TECHNIQUES FOR RCS PREDICTION OF PLATE GEOMETRIES

A. INTRODUCTION

Scattering from a rectangular plate and from simple targets composed of rectangular plates are important and useful problems to study because specific scattering mechanisms can be isolated and closely analyzed. Some of the scattering mechanisms of current interest in developing high-frequency asymptotic modeling techniques are diffractions from electrically thin (thickness $\ll \lambda$), lossy dielectrics backed by a perfect conductor; equivalent impedance representations for this geometry; nonprincipal-plane scattering; and corner diffractions. These topics have been addressed in previous reports [1] - [8]. This part of the report details the continuing work on the problem of scattering from a rectangular plate backed by an electrically thin, lossy dielectric.

To determine the effectiveness of the Uniform Theory of Diffraction (UTD) expressions for a coated wedge, these diffraction coefficients are used to model the principal-plane scattering from a strip/plate geometry coated with a lossy dielectric. The hard polarization case is examined in this report. Terms for higher-order diffractions are included in the model. A breakdown of the various terms is used to determine the contibution of the higher-order terms to the overall radar cross section (RCS). Computed results are compared to measured RCS data for validation.

One of the primary concerns in the modeling of coated conductors is the boundary condition describing the coating. This investigation has focused on using the Impedance Boundary Condition (IBC) and approximating the equivalent impedance of the coating backed by a perfect conductor in terms of a short-circuited transmission-line model [8]. This is considered to be an accurate approximation near and at normal incidence to the surface. In order to verify this, a physical optics (PO) model for the plate is compared to experimental data and to the UTD model.

B. THEORY AND RESULTS

1. Coated Plate UTD RCS Model — Hard Polarization

In the last report [8], UTD coefficients for hard polarization scattering from the coated wedge of Fig. 1 were presented. These coefficients were derived from Griesser and Balanis' UTD coefficients [9] for a general dielectric wedge. Adapting these coefficients for the special case of a coated wedge resulted in simplification of the expressions involved, which led to faster computational times. In a previous report [7], a model for the principal-plane RCS of the coated plate of Fig. 2 was presented. This model used only first-order diffraction terms. Results from this model, shown in the last report [8], revealed good agreement with experimental data near and at normal incidence to the plate. It was thought that the addition of terms to account for higher-order diffractions and surface waves would immensely improve the results away from normal incidence.

Terms to account for second- and third-order diffractions have been added to the RCS model of the coated plate for the hard polarization case. The fields for the various orders of diffraction are given below. An $e^{j\omega t}$ time convention is assumed and suppressed throughout. The incident field is:

Incident Field

$$\mathbf{E_i} = -\hat{a}_\phi E_o e^{jk(x\cos\phi' + y\sin\phi')} \tag{1}$$

The diffracted fields are formed in the usual way for a UTD solution as a product of the incident field, an amplitude spreading factor, a phase factor, and the diffraction coefficient. The necessary diffraction coefficients will not be repeated here as they can be found in the previous report [8]. As has been discussed in the last report, the equivalent impedance of the coated surface is modeled using a short-circuited transmission-line approximation. The appropriate equation is given also in the last report [8].

The first-order diffracted field is:

First-Order Field

$$
\begin{aligned}
\mathbf{E_{d1}} = & -\hat{a}_\phi E_o \sqrt{k} \frac{e^{-jk\rho}}{\sqrt{k\rho}} \left[e^{-j\frac{kw}{2}(\cos\phi' + \cos\phi)} D_{pwff}\left(\psi_1', \psi_1, \theta_0^h, 2\right) \right. \\
& \left. + e^{j\frac{kw}{2}(\cos\phi' + \cos\phi)} D_{pwff}\left(\psi_2', \psi_2, \theta_0^h, 2\right) \right]
\end{aligned}
\tag{2}
$$

$D_{pwff}\left(\psi', \psi, \theta_0^h, n\right)$ refers to the diffraction coefficient for plane-wave incidence, far-field observation. The explicit expression is given in Eq. (15) of the previous report [8]. This coefficient is analogous in form to the Keller GTD diffraction coefficient for perfectly conducting wedges. The parameters needed in Eq. (1) are defined in Figs. 1 and 2, where θ_0^h is the Brewster angle for the coated side of the plate. This is described in Section II.A of [8].

The second- and third-order diffraction terms are expressed in terms of $D_{cwff}\left(d, \psi', \psi, \theta_0^h, n\right)$ and $D_{pwfd}\left(d, \psi', \psi, \theta_0^h, n\right)$, the diffraction coefficients for

4

cylindrical-wave incidence, far-field observation and for plane-wave incidence, observation at a finite distance, respectively. The expression for $D_{cwff}()$ results from the appropriate modification, discussed in Section II.B.3 of [8], of Eq. (16) of [8]. $D_{pwfd}()$ is given by Eq. (16) of [8]. The second- and third-order fields are:

Second-Order Field

$$
\mathbf{E_{d2}} = -\hat{a}_\phi E_o \sqrt{k} \frac{e^{-jk\rho}}{\sqrt{k\rho}} \frac{e^{-jkw}\sqrt{k}}{\sqrt{w}}
$$

$$
\times \left[e^{-j\frac{kw}{2}(\cos\phi'-\cos\phi)} D_{pwfd}\left(w,\psi_1',0°,\theta_0^h,2\right) D_{cwff}\left(w,0°,\psi_2,\theta_0^h,2\right) \right.
$$

$$
\left. + e^{j\frac{kw}{2}(\cos\phi'-\cos\phi)} D_{pwfd}\left(w,\psi_2',0°,\theta_0^h,2\right) D_{cwff}\left(w,0°,\psi_1,\theta_0^h,2\right) \right] \quad (3)
$$

Third-Order Field

$$
\mathbf{E_{d3}} = -\hat{a}_\phi E_o \sqrt{k} \frac{e^{-jk\rho}}{\sqrt{k\rho}} \frac{e^{-j2kw}\sqrt{k}}{w}
$$

$$
\times D_{pwfd}\left(w,0°,0°,\theta_0^h,2\right) D_{cwff}\left(w,0°,0°,\theta_0^h,2\right)
$$

$$
\times \left[e^{-j\frac{kw}{2}(\cos\phi'+\cos\phi)} D_{cwff}\left(w,0°,\psi_1,\theta_0^h,2\right) \right.
$$

$$
\left. + e^{j\frac{kw}{2}(\cos\phi'+\cos\phi)} D_{cwff}\left(w,0°,\psi_2,\theta_0^h,2\right) \right] \quad (4)
$$

The RCS, computed using the preceding fields, is shown in Fig. 3 for a square, coated plate with a width of 2λ. The coating has thickness $t = 0.0423\lambda$ with material parameters $\mu_r = 1.539 - j1.2241$ and $\epsilon_r = 11.826 - j0.16639$. The frequency of operation is 10 GHz. Comparisons are made in Fig. 3 among the measured RCS, the RCS computed using the first-order field of Eq. (1) only, and the RCS computed using the fields of Eqs. (1)-(3). It is obvious that the addition of higher-order diffractions did not improve, or even noticeably change, the modeled RCS

values. The reason for this is shown in Fig. 4, which shows a breakdown of the field contributions. The second- and third-order fields are much smaller than the first-order fields; therefore, they are negligible. During the next reporting period, the surface-wave terms will be added to the model to see if these terms improve the model.

2. Coated Plate PO RCS Model

Thus far, the analysis of the coated plate incorporates a model of the impedance of an electrically thin coating backed by a perfect conductor that uses a short-circuited transmission-line approximation. This is considered a valid and convenient approximation for this geometry [10]; however, the peak experimental and theoretical UTD RCS values on the coated side of the plate do not agree exactly for the example considered in Fig. 3. Reasons for this could be the difficulty in accurately determining the constituitive parameters of the coating material and the extreme sensitivity of the theoretical model to even very small changes in the values of these parameters. Another reason could be inaccuracy in the UTD model. In order to validate the UTD model at this point, a PO model that incorporates the short-circuited transmission-line approximation for the coating impedance was derived for the plate; and the results were compared to the UTD and experimental results.

The PO model was derived in the usual manner [11]. The resulting monostatic RCS equations for the perfectly conducting and coated side of the plate are:

Perfectly Conducting Side

$$\sigma = 4\pi \left(\frac{wL}{\lambda}\right)^2 \cos^2\theta \left(\frac{\sin(kw\sin\theta)}{kw\sin\theta}\right)^2 \tag{5}$$

<u>Coated Side</u>

$$\sigma = 4\pi \left(\frac{wL}{\lambda}\right)^2 \mid \Gamma_r \mid^2 \cos^2\theta \left(\frac{\sin(kw\sin\theta)}{kw\sin\theta}\right)^2 \qquad (6)$$

where w is the plate width, L is the plate length, k is the propagation constant in free space, and θ is the incidence/observation angle measured from the normal to the plate. Γ_r is the reflection coefficient [11] at a material interface with an impedance, η_{eq}. For the results in Fig. 5, η_{eq} is taken as the short-circuited transmission-line equivalence. The expression for this is given in Eq. (1) of the last report [8].

The results in Fig. 5 indicate that the UTD solution incorporating the short-circuited transmission-line approximation is accurate at normal incidence because the model agrees fairly well with the PO model at normal incidence to the coated side of the plate ($\phi = 90°$). The two models differ by approximately 0.84 dB at this point; however, the experimental results at this point are 1.15 dB higher than the PO results, indicating that most of the difference between the UTD and experimental results is due to inaccuracy in characterizing the coating material. It is encouraging to note that the UTD model agrees with the experimental results much better than the PO model in most areas.

C. FUTURE WORK

Future work will focus on three areas — the coated plate, nonprincipal-plane scattering, and the coated dihedral corner reflector. The analysis of the coated plate will be completed so that the UTD model includes both polarizations, surface-wave terms, and surface-wave transition region terms. It may be necessary to explore the use of higher-order boundary conditions to obtain accurate results at scattering angles that are not in the vicinity of normal incidence to the plate. Another area

of consideration will be accurately predicting the scattering at and near grazing incidence, a region which involves overlapping transition regions in which the traditional application of UTD fails.

Nonprincipal-plane scattering from both perfectly conducting and coated plates will be investigated using the Method of Equivalent Currents (MEC) and hybrid techniques. Much work has already been presented on nonprincipal-plane scattering from perfectly conducting plates in previous reports. Future work will involve completing the perfectly conducting plate model by incorporating corner scattering, either in terms of a revised equivalent currents model or through the use of a hybrid technique such as a combination of MEC and Moment Method (MM) or of the UTD and the Finite-Difference Time-Domain (FDTD) technique. Nonprincipal-plane scattering from a coated plate will be investigated using newly developed Incremental Length Diffraction Coefficients (ILDC) for the dielectric wedge [12] and other techniques.

The primary objective of investigating plate scattering is to refine modeling techniques for scattering configurations that are part of more complicated target geometries so that the scattering from complex targets can be more completely understood and predicted using high-frequency techniques. To this end, the work that has been done on scattering from the coated plate will be incorporated into modeling the RCS of a coated dihedral corner reflector. This geometry will eventually serve as a building block in even more complicated geometries.
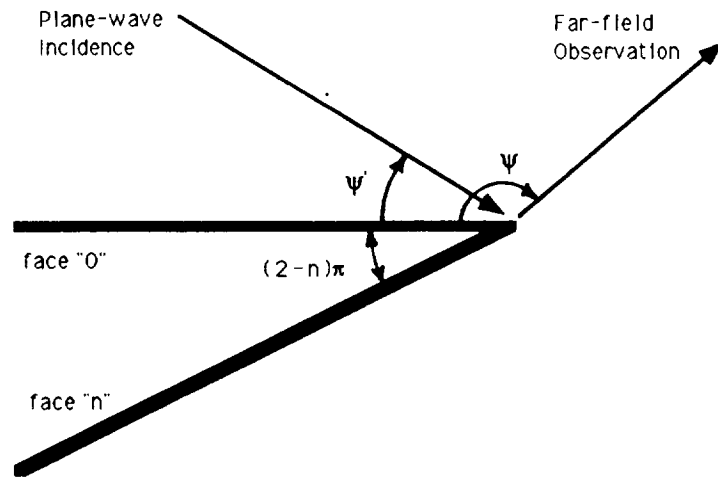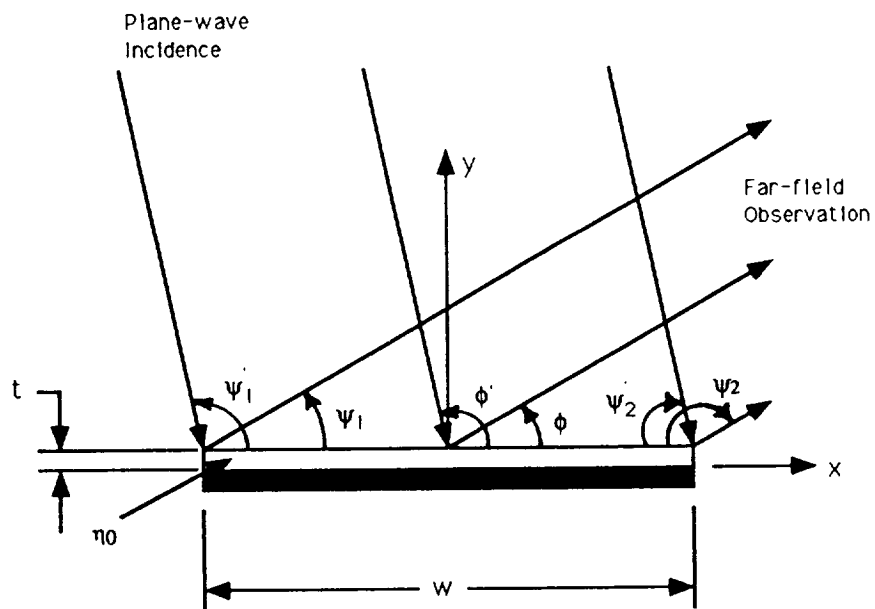
Figure 1: Impedance wedge geometry.

Figure 2: Geometry for principal-plane scattering from a strip/plate with a finite-thickness coating backed by a perfect conductor.
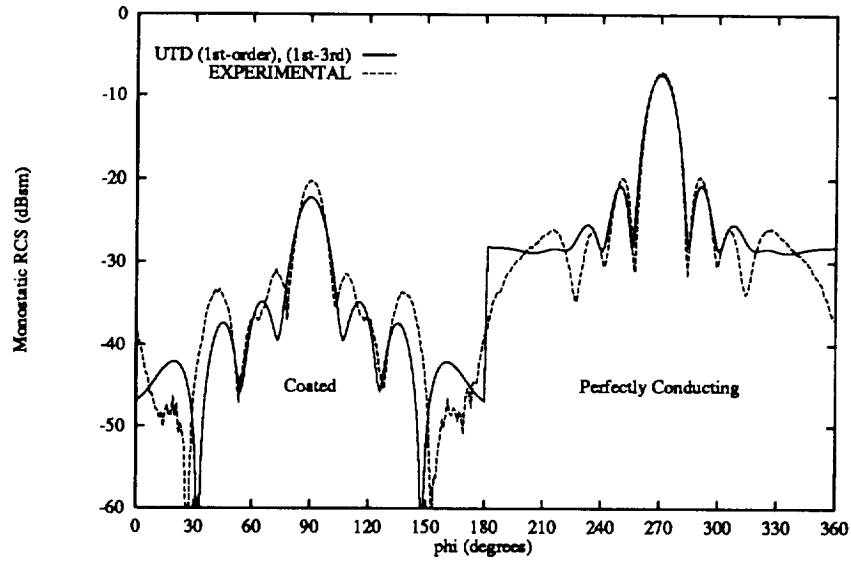
9

Figure 3: Principal-plane monostatic RCS of a coated plate ($w = L = 2\lambda$, $f = 10$GHz, coating: $t = 0.0423\lambda$, $\mu_r = 1.539 - j1.2241$, $\epsilon_r = 11.826 - j0.16639$).

Figure 4: UTD components of the monostatic RCS of a coated plate ($w = L = 2\lambda$, $f = 10$GHz, coating: $t = 0.0423\lambda$, $\mu_r = 1.539 - j1.2241$, $\epsilon_r = 11.826 - j0.16639$).

10

Figure 5: Principal-plane monostatic RCS of a coated plate ($w = L = 2\lambda$, $f = 10\text{GHz}$, coating: $t = 0.0423\lambda$, $\mu_r = 1.539 - j1.2241$, $\epsilon_r = 11.826 - j0.16639$).

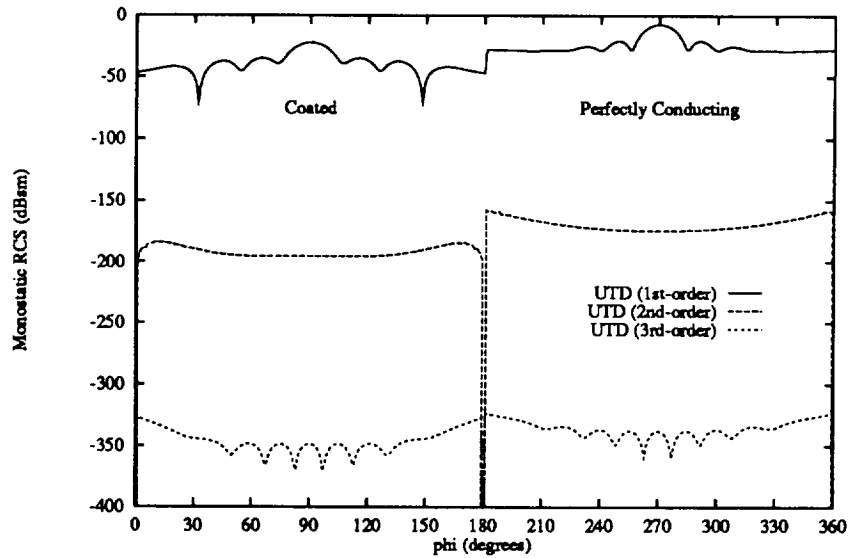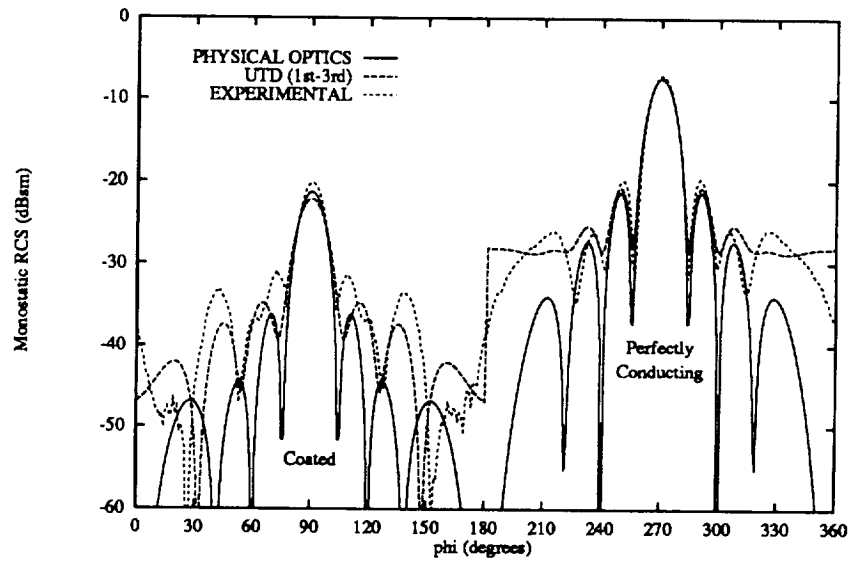# II. A PHYSICAL OPTICS/ EQUIVALENT CURRENTS MODEL FOR THE RCS OF A TRIHEDRAL CORNER REFLECTOR

A. INTRODUCTION

Corner reflectors are very interesting radar targets because they provide a large bistatic or monostatic radar cross section over a broad range of observation angles and frequencies. The two most well-known corner reflectors are the dihedral and the trihedral corner reflectors. The dihedral is formed by the intersection of two flat plates, whereas the trihedral is formed by the intersection of three flat plates. The fact that the trihedral has one plate more than the dihedral is also the reason why its backscatter cross section is much larger than that of the dihedral. In addition, the trihedral has a large radar cross section for any incident angle θ_i, whereas the dihedral has a large radar cross section only for the case where the direction of the incident plane wave is normal to the dihedral axis ($\theta_i = 90°$).

Several researchers in the past have analyzed the scattering properties of dihedral corner reflectors using either Geometrical Optics (GO) together with Geometrical Theory of Diffraction (GTD), or Physical Optics (PO) together with Physical Theory of Diffraction (PTD) [13]-[15]. In all those cases, the direction of incidence was always normal to the dihedral axis and therefore the analysis was carried out as if the object were two-dimensional. On the other hand, the trihedral corner reflector requires a full three-dimensional analysis whose formulation is much more complex than that of the dihedral.

12

In this analysis, Physical Optics (PO) and Method of Equivalent Currents (MEC) were applied on a square trihedral corner reflector to evaluate its monostatic radar cross section. Physical Optics was used for the calculation of first-, second-, and third-order reflections from the trihedral plates, whereas Method of Equivalent Currents was used for the calculation of the first-order diffractions from the edges. It is important to mention that for a relatively large trihedral corner reflector the first-order diffractions are very small compared to the backscatter fields due to internal reflections; therefore, the diffracted fields can be considered negligible. However, as the size of the trihedral becomes smaller, the first order diffractions can contribute significantly to the total backscatter fields. Furthermore, in the analysis of the trihedral corner reflector, it was assumed that higher order diffractions, as well as diffraction-reflections and reflection-diffractions, are negligible.

B. ANALYSIS AND RESULTS

The backscatter cross section of the square trihedral corner reflector, shown in Fig. 6, is evaluated by considering single, double, and triple reflections as well as first-order diffractions. The Physical Optics approximation was used for the calculation of the reflected fields in the far-field region. For the evaluation of the diffracted fields, the Method of Equivalent Currents (MEC), introduced by Michaeli, was applied on the trihedral edges. The entire analysis was carried out for the case of E_θ polarization only.

1. Physical Optics (PO)

Single, double, and triple reflections from the perfectly conducting plates of the square trihedral corner reflector were determined using the Physical Optics approximation

$$\mathbf{J_{po}} = 2\hat{n} \times \mathbf{H^i} \tag{7}$$

13

where $\hat{n}$ is the unit vector normal to the plate under consideration, and $\mathbf{H^i}$ is the incident magnetic field. It is important to point out that the above PO model becomes more accurate as the dimensions of the object increase. After evaluating the surface current density on a particular plate, the vector potential is calculated by

$$\mathbf{A} = \frac{\mu}{4\pi} \int \int_S \mathbf{J_{po}} \frac{e^{-jkR}}{R} ds \simeq \frac{\mu}{4\pi} \frac{e^{-jkr}}{r} \int \int_S \mathbf{J_{po}} e^{jkL_s} ds \tag{8}$$

$$L_s = x \sin \theta_s \cos \phi_s + y \sin \theta_s \sin \phi_s + z \cos \theta_s \tag{9}$$

In the case of monostatic RCS, $\theta_s = \theta_i$ and $\phi_s = \phi_i$. The above integral should be evaluated over the illuminated area of the plate. For single reflections, the illuminated area is the entire square plate, whereas for double and triple reflections, the illuminated area has the shape of a polygon that changes according to the direction of incidence. From the vector potential expression, the corresponding far-field spherical components of the electric field can be calculated using

$$E_\theta = -j\omega A_\theta \qquad and \qquad E_\phi = -j\omega A_\phi \tag{10}$$

The E_r component is considered to be very small and is excluded from the calculations. In most geometries that are used in scattering problems, it is usually more convenient to modify the above general expressions to the ones given below [11].

$$E_r \simeq 0 \tag{11}$$

$$E_\theta \simeq \frac{-jk\eta N_\theta}{4\pi} \frac{e^{-jkr}}{r} \tag{12}$$

$$E_\phi \simeq \frac{-jk\eta N_\phi}{4\pi} \frac{e^{-jkr}}{r} \tag{13}$$

$$N_\theta = \int \int_S (J_x \cos \theta_s \cos \phi_s + J_y \cos \theta_s \sin \phi_s - J_z \sin \theta_s) e^{jkL_s} ds \tag{14}$$

$$N_\phi = \int \int_S (-J_x \sin \phi_s + J_y \cos \phi_s) e^{jkL_s} ds \tag{15}$$

14

The actual expressions for N_θ and N_ϕ are different for each trihedral scattering component. These components, in the case of E_θ polarization, include the following:

Component 1: Single reflection from plate 1

The incident magnetic field on plate 1 is given by

$$\mathbf{H}_1^i = (-\hat{\mathbf{a}}_x \sin \phi_i + \hat{\mathbf{a}}_y \cos \phi_i) H_o e^{jkL_i} \tag{16}$$

$$L_i = x \sin \theta_i \cos \phi_i + y \sin \theta_i \sin \phi_i + z \cos \theta_i \tag{17}$$

The current density on plate 1 due to the incident magnetic field is

$$\mathbf{J}_1 = (-\hat{\mathbf{a}}_x \cos \phi_i - \hat{\mathbf{a}}_y \sin \phi_i) 2 H_o e^{jk(x \sin \theta_i \cos \phi_i + y \sin \theta_i \sin \phi_i)} \tag{18}$$

The corresponding expressions for N_θ and N_ϕ are

$$N_\theta = -2 H_o ab \cos \theta_s (\cos \phi_i \cos \phi_s + \sin \phi_i \sin \phi_s) e^{j(X+Y)} \tag{19}$$
$$\times \ (\frac{\sin X}{X})(\frac{\sin Y}{Y})$$

$$N_\phi = 2 H_o ab (\sin \phi_s \cos \phi_i - \cos \phi_s \sin \phi_i) e^{j(X+Y)} \tag{20}$$
$$\times \ (\frac{\sin X}{X})(\frac{\sin Y}{Y})$$

$$X = \frac{ka}{2} (\sin \theta_s \cos \phi_s + \sin \theta_i \cos \phi_i) \tag{21}$$

$$Y = \frac{kb}{2} (\sin \theta_s \sin \phi_s + \sin \theta_i \sin \phi_i) \tag{22}$$

The integrals in equations (14) and (15) are evaluated over the entire plate, since it is totally illuminated.

Component 2: Single reflection from plate 2

$$\mathbf{H}_2^i = (-\hat{\mathbf{a}}_x \sin \phi_i + \hat{\mathbf{a}}_y \cos \phi_i) H_o e^{jkL_i} \tag{23}$$

15

$$\mathbf{J_2} = \hat{\mathbf{a}}_z 2H_o \cos\phi_i e^{jk(y\sin\theta_i\sin\phi_i + z\cos\theta_i)} \tag{24}$$

$$N_\theta = -2H_o bc \cos\phi_i \sin\theta_s e^{j(Y+Z)}\left(\frac{\sin Y}{Y}\right)\left(\frac{\sin Z}{Z}\right) \tag{25}$$

$$N_\phi = 0 \tag{26}$$

The integration for the evaluation of N_θ was taken over the entire plate.

Component 3: Single reflection from plate 3

$$\mathbf{H_3^i} = (-\hat{\mathbf{a}}_x \sin\phi_i + \hat{\mathbf{a}}_y \cos\phi_i)H_o e^{jkL_i} \tag{27}$$

$$\mathbf{J_3} = \hat{\mathbf{a}}_z 2H_o \sin\phi_i e^{jk(x\sin\theta_i\cos\phi_i + z\cos\theta_i)} \tag{28}$$

$$N_\theta = -2H_o ac \sin\phi_i \sin\theta_s e^{j(X+Z)}\left(\frac{\sin X}{X}\right)\left(\frac{\sin Z}{Z}\right) \tag{29}$$

$$N_\phi = 0 \tag{30}$$

$$Z = \frac{kc}{2}(\cos\theta_s + \cos\theta_i) \tag{31}$$

Like the two previous scattering components, the integration in equation (14) was evaluated on the entire plate in order to obtain N_θ.

Component 4: Double reflection - Plate 1 to Plate 2

The incident magnetic field on plate 1 is given by (16). Then, Geometrical Optics (GO) is used to find the reflected magnetic field from plate 1, which is now the incident magnetic field on plate 2. The use of Geometrical Optics for the first reflection will simplify the final expressions for the doubly reflected fields. If Physical Optics were used to account for the first reflection, instead of Geometrical Optics, then the expression for the scattered field in the far-field region would include a quadruple integral with non-constant limits, which is much more difficult to evaluate than a double integral. The incident magnetic field on plate 2, which was initially reflected from plate 1, is given by

$$\mathbf{H_{12}^i} = (-\hat{\mathbf{a}}_x \sin\phi_i + \hat{\mathbf{a}}_y \cos\phi_i)H_o e^{jkL_{12}} \tag{32}$$

16

$$L_{12} = x \sin \theta_i \cos \phi_i + y \sin \theta_i \sin \phi_i - z \cos \theta_i \tag{33}$$

The current density on plate 2 due to the above magnetic field is

$$\mathbf{J}_{12} = \hat{\mathbf{a}}_z 2H_o \cos \phi_i e^{jk(y \sin \theta_i \sin \phi_i - z \cos \theta_i)} \tag{34}$$

The above expression is valid only on the illuminated area of plate 2. The shape of the illuminated area is a polygon, shown in Fig. 7, whose coordinates can be found accurately, at any angle of incidence, using trigonometric identities. In the case of double reflection from plate 1 to plate 2

$$N_\phi = 0. \tag{35}$$

The expression for N_θ can be found after evaluating the following integral over the illuminated area shown in Fig. 7 (The shape of the illuminated area changes with respect to the incident angle).

$$N_\theta = -2H_o \sin \phi_i \sin \theta_s \int \int_S e^{jk(yW_{y12} + zW_{z12})} ds \tag{36}$$

$$W_{y12} = \sin \theta_s \sin \phi_s + \sin \theta_i \sin \phi_i \tag{37}$$

$$W_{z12} = \cos \theta_s - \cos \theta_i \tag{38}$$

Similar discussion applies for the remaining doubly reflected fields. To save time and space, we present only the necessary equations for those components.

Component 5: Double reflection - Plate 1 to Plate 3

$$\mathbf{H}_{13}^i = (-\hat{\mathbf{a}}_x \sin \phi_i + \hat{\mathbf{a}}_y \cos \phi_i) H_o e^{jkL_{13}} \tag{39}$$

$$L_{13} = x \sin \theta_i \cos \phi_i + y \sin \theta_i \sin \phi_i - z \cos \theta_i \tag{40}$$

$$\mathbf{J}_{13} = \hat{\mathbf{a}}_z 2H_o \sin \phi_i e^{jk(x \sin \theta_i \cos \phi_i - z \cos \theta_i)} \tag{41}$$

$$N_\theta = -2H_o \sin \phi_i \sin \theta_s \int \int_S e^{jk(xW_{x13} + zW_{z13})} ds \tag{42}$$

17

$$N_\phi = 0 \tag{43}$$

$$W_{x13} = \sin\theta_s \cos\phi_s + \sin\theta_i \cos\phi_i \tag{44}$$

$$W_{z13} = \cos\theta_s - \cos\theta_i \tag{45}$$

Component 6: Double reflection - Plate 2 to Plate 1

$$\mathbf{H}_{21}^i = (\hat{\mathbf{a}}_x \sin\phi_i + \hat{\mathbf{a}}_y \cos\phi_i)H_o e^{jkL_{21}} \tag{46}$$

$$L_{21} = -x\sin\theta_i \cos\phi_i + y\sin\theta_i \sin\phi_i + z\cos\theta_i \tag{47}$$

$$\mathbf{J}_{21} = (-\hat{\mathbf{a}}_x \cos\phi_i + \hat{\mathbf{a}}_y \sin\phi_i)2H_o e^{jk(-x\sin\theta_i \cos\phi_i + y\sin\theta_i \sin\phi_i)} \tag{48}$$

$$N_\theta = 2H_o \cos\theta_s(\sin\phi_i \sin\phi_s - \cos\phi_i \cos\phi_s) \tag{49}$$
$$\times \int\int_S e^{jk(xW_{x21} + yW_{y21})}ds$$

$$N_\phi = 2H_o(\cos\phi_i \sin\phi_s - \sin\phi_i \cos\phi_s) \tag{50}$$
$$\times \int\int_S e^{jk(xW_{x21} + yW_{y21})}ds$$

$$W_{x21} = \sin\theta_s \cos\phi_s - \sin\theta_i \cos\phi_i \tag{51}$$

$$W_{y21} = \sin\theta_s \sin\phi_s + \sin\theta_i \sin\phi_i \tag{52}$$

Component 7: Double reflection - Plate 2 to Plate 3

$$\mathbf{H}_{23}^i = (\hat{\mathbf{a}}_x \sin\phi_i + \hat{\mathbf{a}}_y \cos\phi_i)H_o e^{jkL_{23}} \tag{53}$$

$$L_{23} = -x\sin\theta_i \cos\phi_i + y\sin\theta_i \sin\phi_i + z\cos\theta_i \tag{54}$$

$$\mathbf{J}_{23} = -\hat{\mathbf{a}}_z \sin\phi_i 2H_o e^{jk(-x\sin\theta_i \cos\phi_i + z\cos\theta_i)} \tag{55}$$

$$N_\theta = 2H_o \sin\theta_s \sin\phi_i \int\int_S e^{jk(xW_{x23} + zW_{z23})}ds \tag{56}$$

$$N_\phi = 0 \tag{57}$$

18

$$W_{x23} = \sin\theta_s \cos\phi_s - \sin\theta_i \cos\phi_i \tag{58}$$

$$W_{z23} = \cos\theta_s + \cos\theta_i \tag{59}$$

Component 8: Double reflection - Plate 3 to Plate 1

$$\mathbf{H^i_{31}} = (-\hat{\mathbf{a}}_x \sin\phi_i - \hat{\mathbf{a}}_y \cos\phi_i) H_o e^{jkL_{31}} \tag{60}$$

$$L_{31} = x \sin\theta_i \cos\phi_i - y \sin\theta_i \sin\phi_i + z \cos\theta_i \tag{61}$$

$$\mathbf{J_{31}} = (\hat{\mathbf{a}}_x \cos\phi_i - \hat{\mathbf{a}}_y \sin\phi_i) 2H_o e^{jk(x \sin\theta_i \cos\phi_i - y \sin\theta_i \sin\phi_i)} \tag{62}$$

$$N_\theta = -2H_o \cos\theta_s (\sin\phi_i \sin\phi_s - \cos\phi_i \cos\phi_s) \tag{63}$$

$$\times \int\int_S e^{jk(xW_{x21}+yW_{y21})} ds$$

$$N_\phi = -2H_o (\cos\phi_i \sin\phi_s + \sin\phi_i \cos\phi_s) \tag{64}$$

$$\times \int\int_S e^{jk(xW_{x31}+yW_{y31})} ds$$

$$W_{x31} = \sin\theta_s \cos\phi_s + \sin\theta_i \cos\phi_i \tag{65}$$

$$W_{y31} = \sin\theta_s \sin\phi_s - \sin\theta_i \sin\phi_i \tag{66}$$

Component 9: Double reflection - Plate 3 to Plate 2

$$\mathbf{H^i_{32}} = (-\hat{\mathbf{a}}_x \sin\phi_i - \hat{\mathbf{a}}_y \cos\phi_i) H_o e^{jkL_{32}} \tag{67}$$

$$L_{32} = x \sin\theta_i \cos\phi_i - y \sin\theta_i \sin\phi_i + z \cos\theta_i \tag{68}$$

$$\mathbf{J_{32}} = -\hat{\mathbf{a}}_z \cos\phi_i 2H_o e^{jk(-y \sin\theta_i \sin\phi_i + z \cos\theta_i)} \tag{69}$$

$$N_\theta = 2H_o \sin\theta_s \cos\phi_i \int\int_S e^{jk(yW_{y32}+zW_{z32})} ds \tag{70}$$

$$N_\phi = 0 \tag{71}$$

$$W_{y32} = \sin\theta_s \sin\phi_s - \sin\theta_i \sin\phi_i \tag{72}$$

19

$$W_{z32} = \cos\theta_s + \cos\theta_i \qquad (73)$$

The remaining scattering components of the square trihedral corner reflector, besides the edge diffractions, are the triple reflected fields. The triple reflected fields are very important scattering components because they contribute the most to the monostatic radar cross section. The reason is that after three consecutive reflections the reflected fields return directly back to the source. This property of the trihedral corner reflector can be clearly seen if someone applies Geometrical Optics on the three intersected plates and finds the direction of propagation for the triple reflected field. In this analysis, Geometrical Optics was implemented for the calculation of the triple reflections. More precisely, Geometrical Optics was used for the first and second reflections in order to find the expression for the incident field on the third plate; then Physical Optics was applied on the illuminated area of the third plate. As in the case of double reflection, the shape of the illuminated area of the third plate, see Fig. 7, can be determined accurately using trigonometry and vector analysis. Geometrical Optics approximation gives very good results for the monostatic radar cross section of the trihedral, but not very good results for the bistatic radar cross section because the sidelobes are not predicted very well. To get more accurate results for the case of bistatic radar cross section, Physical Optics should be applied for all three consecutive reflections, which is certainly not an easy task to carry out. The reason is because strict application of Physical Optics would require the evaluation of six-fold integrals with non-constant limits. The triply reflected fields of the square trihedral corner reflector are the following.

Component 10: Triple Reflection from Plate 1 to Plate 2 to Plate 3

After applying Geometrical Optics for the first two reflections and the required boundary conditions for the electric field on the conducting plates, the incident

20

magnetic field on the third plate can be found.

$$\mathbf{H}^i_{123} = (\hat{\mathbf{a}}_x \sin\phi_i + \hat{\mathbf{a}}_y \cos\phi_i)H_o e^{jkL_{123}} \tag{74}$$

$$L_{123} = -x\sin\theta_i\cos\phi_i + y\sin\theta_i\sin\phi_i - z\cos\theta_i \tag{75}$$

According to Physical Optics approximation, the surface current density on the illuminated area of the plate 3 is given by

$$\mathbf{J}_{123} = -\hat{\mathbf{a}}_z \sin\phi_i 2H_o e^{jk(-x\sin\theta_i\cos\phi_i - z\cos\theta_i)} \tag{76}$$

The expressions for N_θ and N_ϕ are the following.

$$N_\theta = 2H_o \sin\phi \sin\theta_s \int\int_S e^{jk(xW_{x123} + zW_{z123})}ds \tag{77}$$

$$N_\phi = 0 \tag{78}$$

$$W_{x123} = \sin\theta_s\cos\phi_s - \sin\theta_i\cos\phi_i \tag{79}$$

$$W_{z123} = \cos\theta_s - \cos\theta_i \tag{80}$$

Component 11: Triple Reflection from Plate 1 to Plate 3 to Plate 2

$$\mathbf{H}^i_{132} = (-\hat{\mathbf{a}}_x \sin\phi_i - \hat{\mathbf{a}}_y \cos\phi_i)H_o e^{jkL_{132}} \tag{81}$$

$$L_{132} = x\sin\theta_i\cos\phi_i - y\sin\theta_i\sin\phi_i - z\cos\theta_i \tag{82}$$

$$\mathbf{J}_{132} = -\hat{\mathbf{a}}_z \cos\phi_i 2H_o e^{jk(-y\sin\theta_i\sin\phi_i - z\cos\theta_i)} \tag{83}$$

$$N_\theta = 2H_o \cos\phi_i \sin\theta_s \int\int_S e^{jk(yW_{y132} + zW_{z132})}ds \tag{84}$$

$$N_\phi = 0 \tag{85}$$

$$W_{x132} = \sin\theta_s\sin\phi_s - \sin\theta_i\sin\phi_i \tag{86}$$

$$W_{z132} = \cos\theta_s - \cos\theta_i \tag{87}$$

21

Component 12: Triple Reflection from Plate 2 to Plate 1 to Plate 3

$$\mathbf{H}_{213}^{i} = (\hat{\mathbf{a}}_x \sin \phi_i + \hat{\mathbf{a}}_y \cos \phi_i) H_o e^{jkL_{213}} \tag{88}$$

$$L_{213} = -x \sin \theta_i \cos \phi_i + y \sin \theta_i \sin \phi_i - z \cos \theta_i \tag{89}$$

$$\mathbf{J}_{213} = -\hat{\mathbf{a}}_z \sin \phi_i 2 H_o e^{jk(-x \sin \theta_i \cos \phi_i - z \cos \theta_i)} \tag{90}$$

$$N_\theta = 2 H_o \sin \phi_i \sin \theta_s \int\int_S e^{jk(xW_{x213} + zW_{z213})} ds \tag{91}$$

$$N_\phi = 0 \tag{92}$$

$$W_{x213} = \sin \theta_s \cos \phi_s - \sin \theta_i \cos \phi_i \tag{93}$$

$$W_{z213} = \cos \theta_s - \cos \theta_i \tag{94}$$

Component 13: Triple Reflection from Plate 2 to Plate 3 to Plate 1

$$\mathbf{H}_{231}^{i} = (\hat{\mathbf{a}}_x \sin \phi_i - \hat{\mathbf{a}}_y \cos \phi_i) H_o e^{jkL_{231}} \tag{95}$$

$$L_{231} = -x \sin \theta_i \cos \phi_i - y \sin \theta_i \sin \phi_i + z \cos \theta_i \tag{96}$$

$$\mathbf{J}_{231} = (\hat{\mathbf{a}}_x \cos \phi_i + \hat{\mathbf{a}}_y \sin \phi_i) 2 H_o e^{jk(-x \sin \theta_i \cos \phi_i - y \sin \theta_i \sin \phi_i)} \tag{97}$$

$$N_\theta = 2 H_o \cos \theta_s (\sin \phi_i \sin \phi_s + \cos \phi_i \cos \phi_s) \tag{98}$$

$$\times \int\int_S e^{jk(xW_{x231} + zW_{y231})} ds$$

$$N_\phi = 2 H_o (\sin \phi_s \cos \phi_i - \cos \phi_s \sin \phi_i) \tag{99}$$

$$\times \int\int_S e^{jk(xW_{x231} + zW_{y231})} ds$$

$$W_{x231} = \sin \theta_s \cos \phi_s - \sin \theta_i \cos \phi_i \tag{100}$$

$$W_{z231} = \sin \theta_s \sin \phi_s - \sin \theta_i \sin \phi_i \tag{101}$$

22

Component 14: Triple Reflection from Plate 3 to Plate 1 to Plate 2

$$\mathbf{H^i_{312}} = (-\hat{\mathbf{a}}_x \sin \phi_i - \hat{\mathbf{a}}_y \cos \phi_i)H_o e^{jkL_{312}} \tag{102}$$

$$L_{312} = x \sin \theta_i \cos \phi_i - y \sin \theta_i \sin \phi_i - z \cos \theta_i \tag{103}$$

$$\mathbf{J_{312}} = -\hat{\mathbf{a}}_z \cos \phi_i 2H_o e^{jk(-y \sin \theta_i \sin \phi_i - z \cos \theta_i)} \tag{104}$$

$$N_\theta = 2H_o \cos \phi_i \sin \theta_s \int \int_S e^{jk(yW_{y312}+zW_{z312})} ds \tag{105}$$

$$N_\phi = 0 \tag{106}$$

$$W_{y312} = \sin \theta_s \sin \phi_s - \sin \theta_i \sin \phi_i \tag{107}$$

$$W_{z312} = \cos \theta_s - \cos \theta_i \tag{108}$$

Component 15: Triple Reflection from Plate 3 to Plate 2 to Plate 1

$$\mathbf{H^i_{321}} = (\hat{\mathbf{a}}_x \sin \phi_i - \hat{\mathbf{a}}_y \cos \phi_i)H_o e^{jkL_{321}} \tag{109}$$

$$L_{321} = -x \sin \theta_i \cos \phi_i - y \sin \theta_i \sin \phi_i + z \cos \theta_i \tag{110}$$

$$\mathbf{J_{321}} = (\hat{\mathbf{a}}_x \cos \phi_i + \hat{\mathbf{a}}_y \sin \phi_i)2H_o e^{jk(-x \sin \theta_i \cos \phi_i - y \sin \theta_i \sin \phi_i)} \tag{111}$$

$$N_\theta = 2H_o \cos \theta_s(\sin \phi_i \sin \phi_s + \cos \phi_i \cos \phi_s) \tag{112}$$

$$\times \int \int_S e^{jk(xW_{x321}+zW_{y321})} ds$$

$$N_\phi = 2H_o(\sin \phi_s \cos \phi_i - \cos \phi_s \sin \phi_i) \tag{113}$$

$$\times \int \int_S e^{jk(xW_{x321}+zW_{y321})} ds$$

$$W_{x321} = \sin \theta_s \cos \phi_s - \sin \theta_i \cos \phi_i \tag{114}$$

$$W_{z321} = \sin \theta_s \sin \phi_s - \sin \theta_i \sin \phi_i \tag{115}$$

23

2. Method of Equivalent Currents (MEC)

The Method of Equivalent Currents (MEC), introduced by Michaeli, was applied on the edges of the square trihedral corner reflector to find the first-order diffractions. The expressions for the electric and magnetic currents at the trihedral edges are similar to those published by Michaeli [16, 17]. For completeness, these equations are given below for the specific case of an edge parallel to the z-axis. Similar expressions can be obtained for the edges at other orientations.

$$
M^f = H^i_{zo} \frac{2j\eta}{Nk \sin\beta \sin\beta'} \left[\frac{\sin\phi}{\sin\alpha_1} \frac{\sin((\pi - \alpha_1)/N)}{\cos((\pi - \alpha_1)/N) - \cos(\phi'/N)} \right. \tag{116}
$$

$$
\left. + \frac{\sin(N\pi - \phi)}{\sin\alpha_2} \frac{\sin((\pi - \alpha_2)/N)}{\cos((\pi - \alpha_2)/N) + \cos(\phi'/N)} \right]
$$

$$
I^f = -E^i_{zo} \frac{2j \sin(\phi/N)}{kN\eta \sin^2\beta\prime} \left[\frac{1}{\cos((\pi - \alpha_1)/N) - \cos(\phi'/N)} \right. \tag{117}
$$

$$
\left. + \frac{1}{\cos((\pi - \alpha_2)/N) + \cos(\phi'/N)} \right] - H^i_{zo} \frac{2j}{Nk \sin\beta'}
$$

$$
\cdot \left[\frac{\mu_1 \cot\beta' - \cot\beta \cos\phi}{\sin\alpha_1} \frac{\sin((\pi - \alpha_1)/N)}{\cos((\pi - \alpha_1)/N) - \cos(\phi'/N)} \right.
$$

$$
\left. - \frac{\mu_2 \cot\beta' - \cot\beta \cos N\pi - \phi}{\sin\alpha_2} \frac{\sin((\pi - \alpha_2)/N)}{\cos((\pi - \alpha_2)/N) + \cos(\phi'/N)} \right]
$$

where

$$
\mu_1 = \frac{\cos\gamma_1 - \cos^2\beta'}{\sin^2\beta\prime} \tag{118}
$$

$$
\mu_2 = \frac{\cos\gamma_2 - \cos^2\beta'}{\sin^2\beta\prime} \tag{119}
$$

$$
\cos\gamma_1 = \sin\beta' \sin\beta \cos\phi + \cos\beta' \cos\beta \tag{120}
$$

$$
\cos\gamma_2 = \sin\beta' \sin\beta \cos(N\pi - \phi) + \cos\beta' \cos\beta \tag{121}
$$

$$\alpha_1 = -j\ln(\mu_1 + \sqrt{\mu_1^2 - 1}) \tag{122}$$

$$\alpha_2 = -j\ln(\mu_2 + \sqrt{\mu_2^2 - 1}) \tag{123}$$

The above formulations were applied on the trihedral edges. However, the diffracted fields are relatively small compared to the reflected fields; therefore, they will not contribute very much to the monostatic radar cross section. On the other hand, it is important that these diffractions be included for the bistatic radar cross section, since now the reflected fields will be of lower magnitude and first-order diffractions will be more significant. In our analysis, first-order diffractions were included for both monostatic and bistatic radar cross section, because first-order diffractions become increasingly important as the target becomes smaller; even for the monostatic case.

3. Results

A complex program based on the above formulations has been developed to calculate both monostatic and bistatic RCS of the square trihedral corner reflector for the E_θ polarization. This program is applicable for any angle of incidence and/or observation angle. It also runs very well and fast on various computers such as the SUN, VAX, CMS, or even PC. Two plots for the monostatic case are presented in this report. Fig. 8 shows the monostatic RCS for an incident angle of $\phi = 45^\circ$ as the angle θ varies from 0° to 90°. Fig. 9 shows the monostatic RCS for an incident angle $\theta = 66^\circ$ as the angle ϕ varies from 0° to 90°. For both plots, the size of each square trihedral plate was taken to be 5λ. FDTD data were provided to compare our results. Comparison between the two methods shows a very good agreement. In addition, it is important to note that running an FDTD program to calculate

the monostatic RCS of a trihedral definitely requires a lot of time, whereas running the "PO + MEC" program to do the same task takes only a few seconds.

C. FUTURE WORK

In this report, only the monostatic RCS of the square trihedral corner reflector in the E_θ polarization was discussed. Actually, the formulations given in the above sections can be used for bistatic RCS without any modification. However, we do not present any plots for the bistatic RCS because of lack of accuracy at the sidelobes. There is very good agreement with FDTD data at and near the mainlobe but not very good agreement at the sidelobes. The reason is because the Geometrical Optics approximation was used for both double and triple reflections. To get better graphs for the bistatic case, it is necessary that we use strictly Physical Optics for double and trible reflections. However, this is a very challenging task, since it would be necessary to solve a quadruple and a six-fold integral with non-constant limits. This will be a priority goal for the future. In addition, the formulation for the E_ϕ polarization will be investigated to have a complete picture of the backscattering of the square trihedral corner reflector. Lastly, a similar procedure will be applied for a triangular trihedral corner reflector. Measurements will also be performed to compare with predictions.
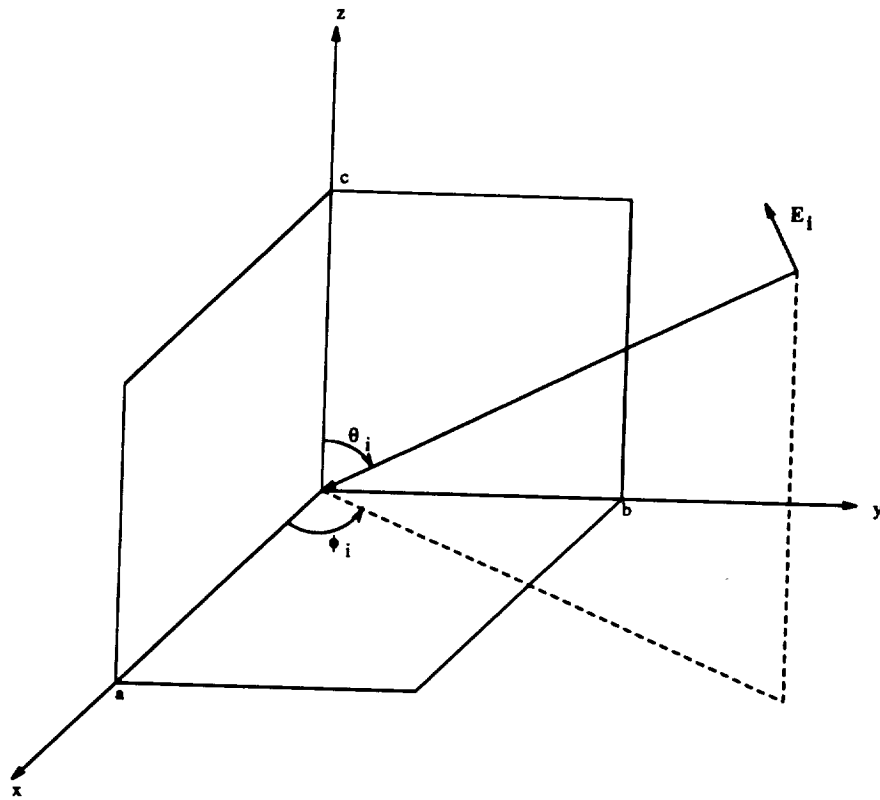
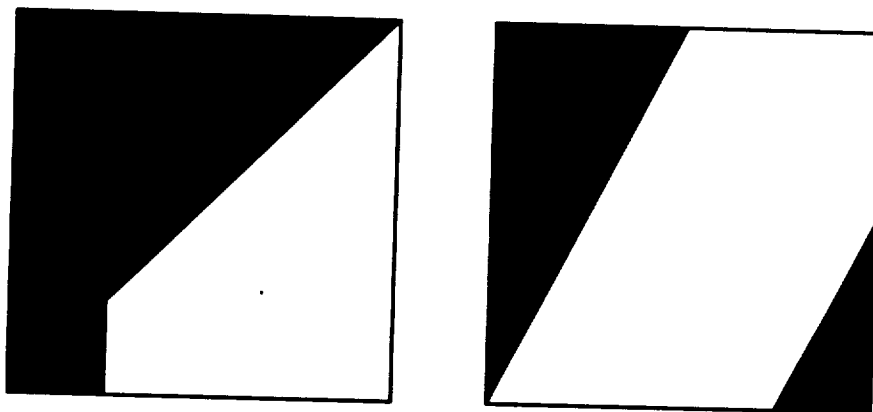Figure 6: Geometry of the trihedral corner reflector.

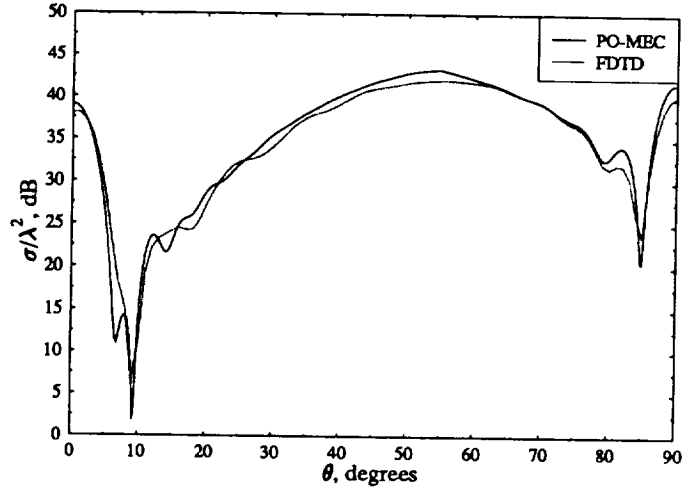Figure 7: Shading of a trihedral plate from doubly and triply reflected fields.

Figure 8: Monostatic RCS of the square trihedral corner reflector with dimensions $a = b = c = 5.0\lambda$, incident angle $\phi = 45°$, and polarization of the E-field in the theta direction.

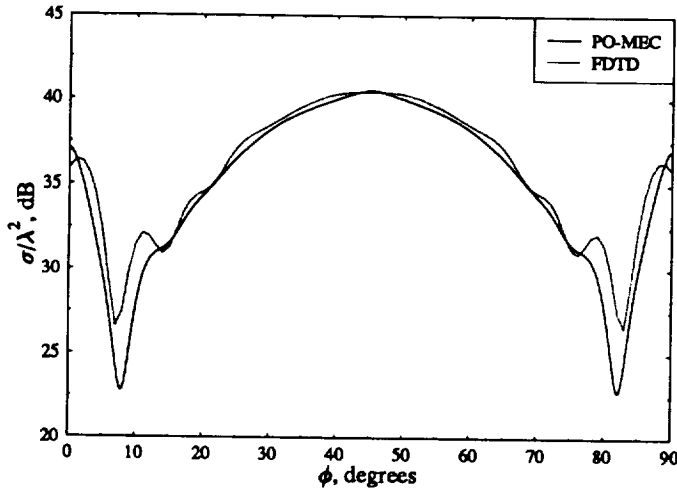Figure 9: Monostatic RCS of the square trihedral corner reflector with dimensions $a = b = c = 5.0\lambda$, incident angle $\theta = 66°$, and polarization of the E-field in the theta direction.

28

References

[1] C. A. Balanis and L. A. Polka, "Nonprincipal plane scattering of flat plates," Semiannual Report, Grant No. NAG-1-562, National Aeronautics and Space Administration, Langley Research Center, Hampton, VA, Jan. 31, 1989.

[2] C. A. Balanis and L. A. Polka, "Nonprincipal plane scattering from flat plates — second-order and corner diffraction," Semiannual Report, Grant No. NAG-1-562, National Aeronautics and Space Administration, Langley Research Center, Hampton, VA, Jul. 31, 1989.

[3] C. A. Balanis, L. A. Polka, and K. Liu, "Nonprincipal plane scattering from rectangular plates and pattern control of horn antennas," Semiannual Report, Grant No. NAG-1-562, National Aeronautics and Space Administration, Langley Research Center, Hampton, VA, Jan. 31, 1990.

[4] —, "Scattering from coated structures and antenna pattern control using impedance surfaces," Semiannual Report, Grant No. NAG-1-562, National Aeronautics and Space Administration, Langley Research Center, Hampton, VA, Jul. 31, 1990.

[5] C. A. Balanis and L. A. Polka, "High-frequency techniques for RCS prediction of plate geometries," Semiannual Report, Grant No. NAG-1-562, National Aeronautics and Space Administration, Langley Research Center, Hampton, VA, Jan. 31, 1991.

[6] —, "High-frequency techniques for RCS prediction of plate geometries," Semiannual Report, Grant No. NAG-1-562, National Aeronautics and Space Administration, Langley Research Center, Hampton, VA, Jul. 31, 1991.

[7] —, "High-frequency techniques for RCS prediction of plate geometries," Semiannual Report, Grant No. NAG-1-562, National Aeronautics and Space Administration, Langley Research Center, Hampton, VA, Jan. 31, 1992.

[8] —, "High-frequency techniques for RCS prediction of plate geometries," Semiannual Report, Grant No. NAG-1-562, National Aeronautics and Space Administration, Langley Research Center, Hampton, VA, Jul. 31, 1992.

[9] T. Griesser and C. A. Balanis, "Reflections, diffractions, and surface waves for an impedance wedge of arbitrary angle," *IEEE Trans. Antennas Propagat.* , vol. AP-37, pp. 927-935, Jul. 1989.

[10] E. H. Newman and M. R. Schrote, "An open surface integral formulation for electromagnetic scattering by material plates," *IEEE Trans. Antennas Propagat.* , vol. AP-32, Jul. 1984.

[11] C. A. Balanis, "Advanced Engineering Electromagnetics". New York: John Wiley and Sons, 1989.

[12] G. Pelosi, S. Maci, R. Tiberio, and A. Michaeli, "Incremental length diffraction coefficients for an impedance wedge," *IEEE Trans. Antennas Propagat.* , vol. AP-40, pp. 1201-1210, Oct. 1992.

[13] T. Griesser and C. A. Balanis, "Dihedral corner reflector backscatter using higher order reflections and diffractions," *IEEE Trans. Antennas Propagat.* , vol. AP-35, pp. 1235-1247, Nov. 1987.

[14] —, "Backscatter analysis of dihedral corner reflectors using physical optics and the physical theory of diffraction," *IEEE Trans. Antennas Propagat.* , vol. AP-35, pp. 1137-1147, Oct. 1987.

[15] E. F. Knott, "RCS reduction of dihedral corners," *IEEE Trans. Antennas Propagat.* , vol. AP-25, pp. 406-409, May 1977.

[16] A. Michaeli, "Equivalent edge currents for arbitrary aspects of observation," *IEEE Trans. Antennas and Propagat.* , vol. AP-32, pp. 252-258, Mar. 1984.

[17] A. Michaeli, "Elimination of infinities in equivalent edge currents, part i: Fringe currents," *IEEE Trans. Antennas Propagat.* , vol. AP-34, pp. 912-918, Jul. 1986.